

Fabrication of (111)-Faced Single-Crystal Diamond Plates by Laser Nucleated Cleaving

Samuel M. Parks^a, Richard R. Grote^a, David A. Hopper^{a,b}, Lee C. Bassett^{a,*}

^aQuantum Engineering Laboratory, Department of Electrical & Systems Engineering,
University of Pennsylvania, Philadelphia, PA 19104, United States

^bDepartment of Physics, University of Pennsylvania, Philadelphia, PA 19104, United States

Abstract

Single-crystal diamond plates with surfaces oriented in a (111) crystal plane are required for high-performance solid-state device platforms ranging from power electronics to quantum information processing architectures. However, producing plates with this orientation has proven challenging. In this paper, we demonstrate a method for reliably and precisely fabricating (111)-faced plates from commercially available, chemical-vapor-deposition-grown, type-IIa single-crystal diamond substrates with (100) faces. Our method uses a nanosecond-pulsed visible laser to nucleate and propagate a mechanical cleave in a chosen (111) crystal plane, resulting in faces as large as $3.0\text{ mm} \times 0.3\text{ mm}$ with atomically flat surfaces, negligible miscut angles, and near zero kerf loss. We discuss the underlying physical mechanisms of the process along with potential improvements that will enable the production of millimeter-scale (111)-faced single-crystal diamond plates for a variety of emerging devices and applications.

Keywords: single-crystal diamond, cleaving, (111) orientation, surface roughness

1. Introduction

Advances in homoepitaxial chemical vapor deposition (CVD) of high-purity single-crystal diamond (SCD) have made the exceptional material properties of SCD available for a variety of new and exciting applications [1–4]. In particular, the wide bandgap, high carrier mobility, large thermal conductivity, corrosion resistance, and biocompatibility of SCD have enabled new devices for high-power electronics [5], ultraviolet light sources [6] and detectors [7], nonlinear optics [8–10], quantum information processing [11], biomedical applications [12, 13], magnetometry [14], and integrated photonics [15–19].

Many of these diverse applications benefit from the advantageous mechanical, thermal, and bond properties along $\langle 111 \rangle$. For example, the (111) crystal plane is the hardest face [20, 21], making it more resilient to damage and desirable for industrial scale diamond cutting tools [1]. Similarly, the Raman gain coefficient is strongest when the optical polarization axis is aligned along $\langle 111 \rangle$ [22, 23]. For this reason, integrating on-chip Raman lasers requires precise crystallographic orientation of the diamond layer to maximize the laser efficiency [10]. High-power electronic devices also benefit from (111) faces, which provide improved donor incorporation efficiency and correspondingly higher mobility [5, 24–28]. Finally, point defects in SCD that are used as single-photon sources and spin

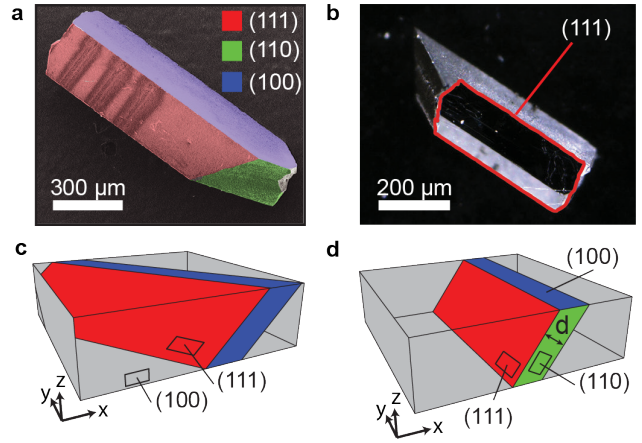


Figure 1: Laser-nucleated cleaving of single crystal diamond. (a) Scanning electron micrograph and (b) bright-field optical image of (111)-faced plates produced from a standard grade (SG) (100)-faced single-crystal diamond. Illustration of the orientation of a (111)-faced plate that can be produced from (c) an SG (100)-faced sample with (100) sides and (d) an electronics grade (EG) sample with (110) sides.

qubits, such as the nitrogen-vacancy and silicon-vacancy centers, have a symmetry axis aligned along $\langle 111 \rangle$ directions [29–32]. Thus, a (111) face maximizes the interaction with normally-incident light fields and optimizes the photon collection efficiency from these emitters, which is critically important for light-matter quantum interfaces [33] and high-sensitivity magnetometry [34, 35].

*Corresponding author.

Email address: lbassett@seas.upenn.edu (Lee C. Bassett)

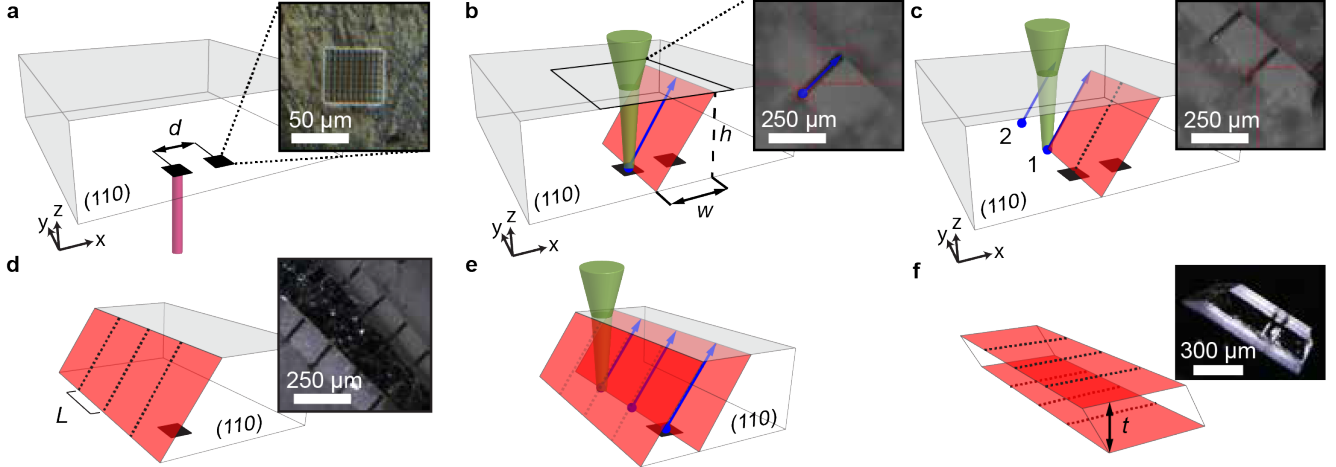


Figure 2: **LNC process overview.** Laser-nucleated cleaving process for an EG-SCD starting plate with (100) top and bottom faces and (110) side walls. (a) Fabrication of textured nucleation sites produced with a UV Excimer laser. (b) A (111) cleavage plane is generated by focusing the laser below the bottom surface and rastering away from a nucleation site in the x -direction. (c) The (111) cleavage plane is extended by repeating the laser raster at discrete steps in y . (d) Illustration of the complete cleave for a single (111) face. (e), (f) The process is repeated for an adjacent nucleation site in order to cleave a plate with parallel (111) faces.

While (100)-faced SCD plates are commonly produced by homoepitaxial CVD, growth of (111)-faced SCD plates has proven challenging due to twinning and stacking faults that form along $\langle 111 \rangle$ directions [2, 28, 36]. Despite some recent advances [4, 37], inherent challenges still remain in growing (111)-oriented layers thicker than ≈ 100 nm with low surface roughness. For this reason, macroscopic (111)-faced plates are typically cut from larger (100)-faced starting plates using micro-machining laser ablation tools [38] and subsequent polishing steps are used to reduce the surface roughness [39, 40]. This process results in substantial loss of costly SCD material (kerf loss) along with misalignment of the resulting face relative to $[111]$, since it is nearly impossible to polish the (111) face using traditional methods [20]. Furthermore, the mechanical polishing step induces sub-surface damage that can only be removed by further chemical etching [36].

An alternate approach, traditionally used to shape diamond gemstones, is mechanical cleaving, where a small scribe, or kerf, is created and struck by hand with a knife to initiate a cleave. It is not feasible, however, to perform this process by hand with the micron-scale accuracy needed to create large, thin, parallel plates for electronic and optical applications from small samples of SCD. Instead, it would be valuable to establish a process similar to silicon stealth dicing [41], whereby a laser is used to nucleate and propagate a mechanical cleave with high spatial precision and control of the cleaving dynamics.

In this paper, we present a laser-nucleated cleaving (LNC) process for SCD. Rather than machining the entire surface of a desired face, the LNC process uses a pulsed, focused laser with sub-bandgap photon energy (532 nm) to locally graphitize a thin (≈ 30 μ m diameter) line that propagates a mechanical cleave along a desired (111) plane. As

shown in Fig. 1, (111)-faced plates are fabricated by generating two parallel (111) cleave planes, forming a parallelepiped shape. This process results in large, atomically-flat (111)-faced SCD plates while eliminating kerf loss and removing the need for mechanical polishing.

The paper is organized as follows: first, a step-by-step description of the LNC process is provided, followed by atomic force microscopy (AFM) and X-ray diffraction measurements that determine the surface roughness and confirm the crystal orientation, respectively. Then, the potential physical mechanisms that contribute to the LNC process are discussed. Finally, avenues for improving the process to optimize the size and flatness of (111)-faced SCD plates are presented.

2. Materials and methods

The LNC process is illustrated in Fig. 2 and the individual steps are described in the section below. We begin by discussing the types of SCD plates used in this study followed by the micro-machining laser specifications. Then, we outline the LNC process which is grouped into four subprocesses consisting of nucleation site creation, initiation of the cleave, propagating the cleave front, and backside cleaving to produce a free standing (111)-faced SCD plate. Finally, the details concerning the characterization of the SCD plates' physical properties are covered. Additional details are included in the supporting information [42].

2.1. Materials

We perform LNC on commercially available “standard grade” (SG, < 1 ppm nitrogen and boron) and high-purity “electronics grade” (EG, < 5 ppb nitrogen and boron) type-IIa, CVD single-crystal diamond from Element6 [43].

The edge and face orientations of these samples are shown in Fig. 1(c)-(d).

2.2. Nucleation site creation

The LNC process begins with the creation of a nucleation site on the bottom surface of the starting SCD plate. The nucleation site acts as a seed for producing the initial cleave. For samples with two polished (100) faces, textured regions [Fig. 2(a), inset] are laser-machined onto the backside using an excimer laser [42]. Only one textured site per desired (111) face is required. For single-side polished pieces, the unpolished side of as-received samples with a surface roughness of $R_q = 250$ nm [43] was found to be sufficient to nucleate cleaves without any additional patterning.

2.3. Micromachining laser beam preparation

We perform LNC using a nanosecond pulsed, frequency-doubled Yb-doped fiber laser operating at a wavelength of 532 nm with a repetition rate of 150 kHz, integrated in a micromachining laser system (IPG Photonics, IX-280-ML). The primary focusing optic is a 100 mm-focal-length objective that produces a beam waist of diameter < 17 μ m, a beam quality factor of $M^2 = 1.5$, and a depth of field ≈ 800 μ m. In this system, the laser focus and course lateral position are controlled using a motorized stage, and cuts are made by steering the beam with a galvo scanner. The starting SCD plate is fixed to a 1.0 mm-thick glass microscope slide with double-sided tape so that the micromachining laser can be focused through the air/diamond interface (referred to as the top surface) onto the tape-diamond interface (referred to as the bottom surface).

The beam focus is positioned such that the bottom surface of the SCD plate ablates while the top surface does not. SCD ablation by sub-bandgap light is a nonlinear optical process, and the ablation rate depends sensitively on the pulse fluence [44]. Positioning the laser focus close to the bottom surface establishes a fluence gradient such that the top surface is unaffected by the micromachining laser beam, whereas the bottom surface is above the threshold for ablation and graphitization. The presence of a nucleation site or unpolished bottom surface further lowers the threshold for ablation. Figure 3 depicts the experimentally measured ablation rate of a top polished SCD surface as a function of pulse energy for our micromachining laser, exhibiting an abrupt threshold around 140 μ J.

2.4. Initiating the cleave

To initiate a cleave, the micromachining laser beam is aligned over a textured nucleation site, or a target region of an unpolished bottom surface using the sample stage. The laser beam is then switched on and laterally scanned in x at a speed of 8 cm s^{-1} by a distance w , as illustrated in Fig. 2(b). The scan distance is calculated according to $w = h / \tan 55^\circ$, where h is the starting SCD plate thickness, and 55° is the angle between the [111] and

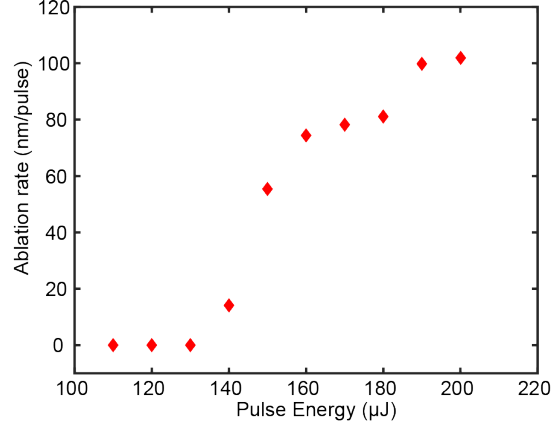


Figure 3: **Ablation rate.** Measured ablation rate as a function of laser pulse energy, when focused at the diamond surface.

[100] lattice vectors. This translation distance ensures that the cleave extends through the full thickness of the SCD (x - z plane). After this step, a darkened line appears and a new reflective surface can be seen within the diamond [Fig. 2(b), inset]. The combination of these two observations heralds the presence of a cleave along a (111) face.

2.5. Propagating the cleave

As seen in Fig. 2(b), a typical cleave only propagates a few hundred microns away from the laser scan line in the y -direction. The (111) crystal face is extended by repeating the lateral laser scans used in the previous step, but with the beam translated along y near the edge of the newly-created (111) face. Scanning the laser again along x extends the cleave further along y , as shown in Fig. 2(c). As such, a textured nucleation site is only required at the position of the first laser scan line to initiate a cleavage plane. After each subsequent extension of the (111) face, a new boundary is identified in the microscope and the laser scan process is repeated until the cleave has been extended across the entire width of the starting SCD plate, creating a fully exposed (111) face [Fig. 2(d)].

2.6. Backside cleaving

To complete the (111)-faced SCD plate fabrication, a second (111) crystal face is generated that is parallel to the initial exposed face. The distance between the two nucleation sites sets the resulting plate thickness t as can be seen in Fig. 2(f). For reliable performance, we find that the second nucleation site should be offset by a distance greater than the beam translation distance, ($d > w$) [Fig. 2(e)], hence the minimum (111)-faced plate thickness is limited by the starting plate height, h .

2.7. Characterization

Measurements of the cleaved-face lattice orientation were made at room temperature using X-Ray diffraction with a $\lambda = 0.1544$ nm source, a 1° divergence slit, 1°

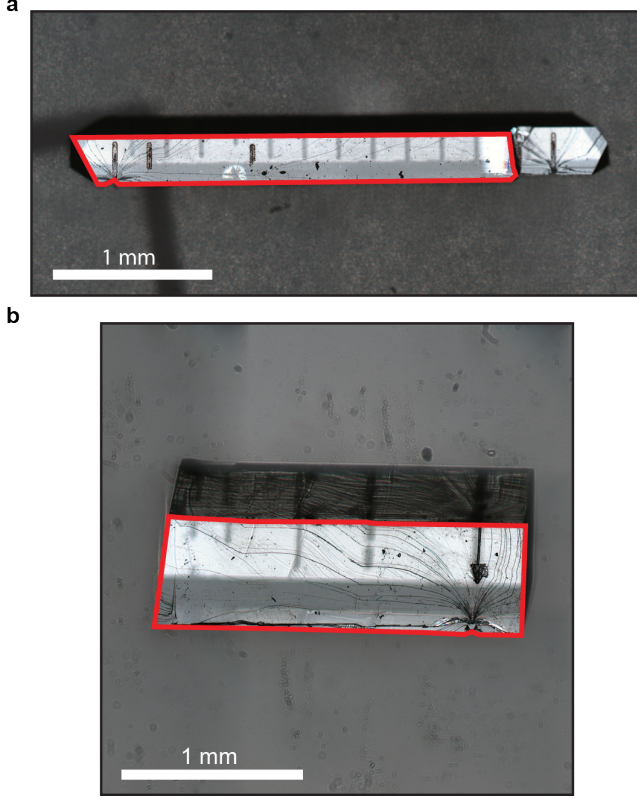


Figure 4: **SCD (111)-faced plates fabricated by LNC.** Bright-field microscope images of (a) a $3\text{ mm} \times 0.3\text{ mm} \times 0.17\text{ mm}$ -thick SG-SCD plate and (b) a $2.0\text{ mm} \times 0.6\text{ mm} \times 0.52\text{ mm}$ -thick EG-SCD plate. Top (111)-faces are outlined in red.

scatter slit, 0.6 mm receiving slit, and a scintillator detector. Plates were mounted on a glass slide using crystal bond. Surface roughness was characterized using an Asylum MFP-3D atomic-force scanning probe with z -axis noise $< 0.06\text{ nm}$ (average deviation) in a 0.1 Hz-1 kHz bandwidth.

3. Results

3.1. Plate dimensions

Representative (111)-faced plates produced by the LNC process are shown in Fig. 1(a)-(b), Fig. 2(f), and Fig. 4. The dark lines on the top and bottom surfaces of the plates are the locations of the micromachining laser scan lines. A laser-scan-line separation in y of $L = 300\text{ }\mu\text{m}$ was found to be suitable for reliably propagating the cleave using an automated process [Fig. 4, bottom surface]. However, by manually identifying the cleavage plane boundary in the microscope, much larger spacings can be realized [Fig. 4, top surface], resulting in laser-scan-line-free areas ranging from 0.18 mm^2 [Fig. 2(f) inset] to 1.2 mm^2 [Fig. 4(b)].

Fabricated plate thicknesses vary from $50\text{ }\mu\text{m}$ [Fig. 2(f) inset] to $520\text{ }\mu\text{m}$ [Fig. 4(b)]. Minimum thicknesses of $170\text{ }\mu\text{m}$

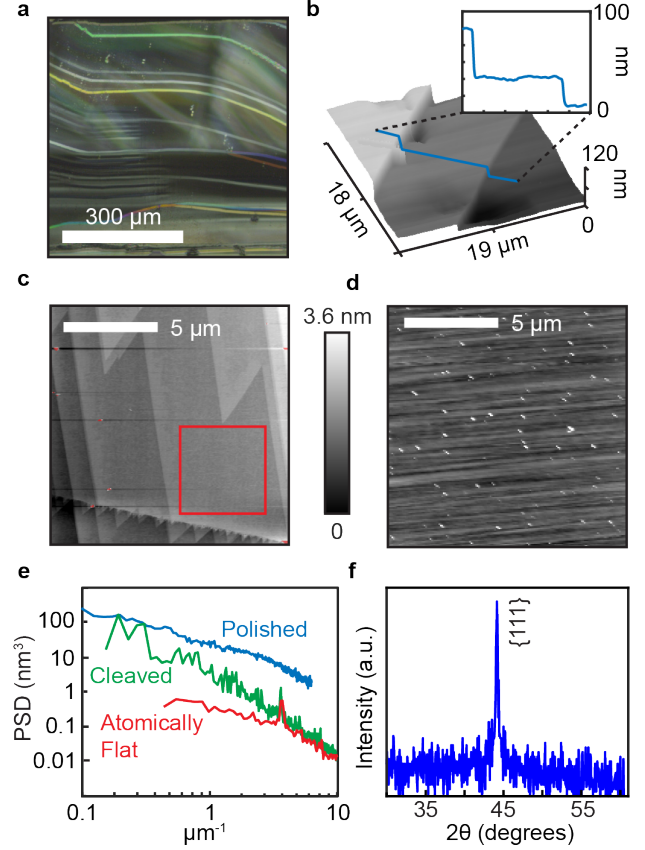


Figure 5: **Surface morphology.** (a) Differential-interference contrast image of an LNC, EG-SCD plate showing Wallner lines on the cleaved surface. (b) Atomic-force micrograph area scan and profile line-scan inset of Wallner lines. (c) Atomic-force micrograph of atomic step edges found in the area between Wallner lines. (d) Atomic-force micrograph of the as-received EG-SCD polished surface. (e) 1D power spectra extracted from the AFM micrographs in (c) and (d) as well as the cropped region on an atomically-flat terrace in (c). (f) X-ray diffraction curve verifying that the face of the plate is (111)-oriented.

and $290\text{ }\mu\text{m}$ are reliably produced for starting plate thicknesses of $300\text{ }\mu\text{m}$ and $500\text{ }\mu\text{m}$, respectively. A single $3\text{ mm} \times 3\text{ mm}$ (100) SCD plate can typically yield up to 10 (111)-faced plates. The number is limited due to the increasing number of stochastically-generated cracks along undesired planes as the original SCD plate is diced into multiple (111)-faced plates.

3.2. Surface Morphology

Lines running along the (111) face in the direction of the cleave propagation can be observed in the differential-interference-contrast optical microscope image shown in Fig. 5(a). These nanometer-scale steps or ridges are known as Wallner lines, which appear ubiquitously on cleaved surfaces of brittle materials as a result of the interaction between the crack front and transverse acoustic waves [39, 45]. Using atomic force microscopy (AFM), we find

that the Wallner lines typically exhibit step heights of 10–50 nm [Fig 5(b)], with separations that vary from $\approx 10\text{ }\mu\text{m}$ near the initial laser scan line to $>100\text{ }\mu\text{m}$ in regions farther away.

As shown in Fig. 5(c), the areas between Wallner lines exhibit atomically-flat (111) surfaces characterized by micron-scale, triangular terraces with step heights consistent with the expected 0.206 nm spacing of (111) atomic planes [4]. The terraces are occasionally intersected by linear features as observed in the bottom-left of Fig. 5(c). For comparison, the polished (100) surface of an EG-SCD plate, as-received from the manufacturer [43] following cleaning using an acid bath and O_2 plasma treatment, is displayed in Fig. 5(d).

Clearly, the morphologies of the cleaved and polished surfaces are very different. Figure 5(e) shows the power spectral density (PSD) of the AFM scans in Figs. 5(c,d), as well as the PSD for the region of a single atomic plateau indicated by a red box in Fig. 5(c). Over the entire $12\text{ }\mu\text{m} \times 12\text{ }\mu\text{m}$ AFM scan windows, we calculate root-mean-square (RMS) surface roughness values of $R_q = 0.22\text{ nm}$ and 0.46 nm for the cleaved (111) and polished (100) surfaces, respectively. The LNC surface roughness represents an order-of-magnitude improvement compared to the manufacturer’s specification for the polished surface (average roughness $<5\text{ nm}$) and a smoothness comparable to the best values reported from advanced polishing techniques of $<0.1\text{ nm}$ [46]. Furthermore, the majority of the cleaved-surface roughness occurs in the form of atomic steps with micron-scale spacings, whereas the polished surface exhibits roughness over a broad range of spatial frequencies. The calculated RMS roughness of the $25\text{ }\mu\text{m}^2$ region on an atomic terrace is $R_q = 0.05\text{ nm}$, corresponding to the noise floor of the AFM tool. Further details the AFM surface roughness analysis are provided in the supporting information [42].

3.3. Face Orientation

Crystallographic faces were indexed using X-ray diffraction [Fig. 5(f)], showing a peak at $2\theta = 44^\circ$ that corresponds to first order Bragg diffraction from $\{111\}$ planes. Since the spacing between individual (111) planes is $d = a/\sqrt{3} = 0.206\text{ nm}$, where $a = 0.357\text{ nm}$ is the lattice constant of diamond, the first (111) diffraction peak should appear at $2\theta = 2\sin^{-1}(\lambda/(2d)) = 44.0^\circ$. These measurements have insufficient accuracy to determine the miscut angle, but we can use the features in AFM scans like Fig. 5(b)-(c) to estimate the miscut based on the heights and spacings of atomically-flat plateaus. In between Wallner lines, we typically observe atomic terraces with $\approx 2\text{ }\mu\text{m}$ spacings, corresponding to a miscut angle of $\sim 0.006^\circ$. Over larger length scales, Wallner lines of height $\approx 50\text{ nm}$ are typically separated by $\approx 10\text{ }\mu\text{m}$, corresponding to an overall miscut angle $\approx 0.3^\circ$ [42].

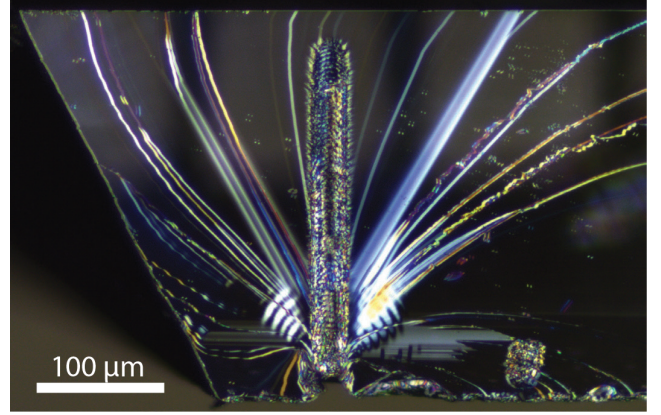


Figure 6: **Cleave nucleation.** Circularly-polarized differential interference contrast (CDIC) image of the first cleave line on an SG-SCD (111) face, illustrating how Wallner lines emanate from the laser line.

4. Discussion

While further studies are required to fully elucidate the physics underlying the LNC process, the observation of dark laser-induced lines in Figs. 1(a), 2, and 4 suggest that the LNC process initiates and propagates a graphitization wave with a sufficiently large diameter to locally stress the SCD beyond its fracture threshold. In effect, LNC is a mechanical cleaving process in which the laser acts as a sub-micron knife striking a kerf, with the potential for creating large-area, atomically flat faces in SCD plates and gemstones for a variety of applications.

Pulsed-laser graphitization and laser-guided graphitization wave propagation in SCD have been studied extensively in the context of 3D-laser writing [40]. In LNC, graphitization waves are propagated by focusing the laser through the starting SCD plate such that the beam fluence is sufficiently large at the bottom surface nucleation site to initiate graphitization, while the defocused beam throughout the bulk of the SCD does not create any material damage, as illustrated in Fig. 3. Once the graphitization wave is initiated at the nucleation site, the ablation threshold drops abruptly such that the fluence required to propagate the wave is much lower than the bulk graphitization threshold [40], allowing for the wavefront to be guided along a (111) plane by laterally scanning the laser in the x -direction as indicated in Fig. 2. Using the appropriate laser fluence, spot size, and scan speed, we are able to create a graphite wave with a sufficiently large transverse diameter to fracture SCD as it propagates in a (111) plane.

Local crack formation from laser-guided graphitization waves has been previously observed in diamond [47], and has been attributed to the substantially greater specific volume (lower density) of graphite as compared to SCD, resulting in strong tensile stresses in the vicinity of the graphitized region. Assuming that the laser can provide adequate fluence, the requirement for producing sufficiently

large internal stresses to cause cracking is determined by the area and speed of graphite generation. Romano *et al.* developed an empirical threshold for crack propagation of $V\pi d^2/4R < 20 \mu\text{m}^3$ per laser shot, where V is the laser scan speed, d is the laser spot size, and R is the pulse repetition rate [40]. The laser micromachining system used for our LNC process has a minimum spot size $d \lesssim 17 \mu\text{m}$ and a scan speed of $V = 8 \text{ cm s}^{-1}$ with a laser pulse repetition rate of 150 kHz, which gives a value of $V\pi d^2/4R \approx 120 \mu\text{m}^3$ per laser shot. The fact that our processing parameters are well above the threshold for exceeding the tensile strength of SCD provides further evidence that laser-guided graphitization waves are the dominant physical mechanism behind LNC. Since SCD preferentially cleaves along $\{111\}$ planes [39] due to the tensile strength being lowest along $\langle 111 \rangle$ directions [48], the graphitization wave and resultant cleave are self guiding along the chosen (111) surface, even though the laser focus is fixed below the sample throughout the entire scan.

In contrast to traditional mechanical cleaving of diamond, LNC provides the opportunity for precise control of the cleave propagation by tuning the scan speed of the laser. Similar to what has been done with silicon stealth dicing [49], where the laser power and stage translation speed have been tuned to achieve Wallner-line-free cleaves [50], further analysis of the mechanisms involved in LNC should allow for drastic reduction of the Wallner lines that form during crack propagation [39]. Furthermore, by simultaneously scanning the laser position and focus, it may be possible to propagate cleaves along $\{100\}$ or $\{110\}$ planes in SCD.

The precision and flexibility of the LNC process will make it useful for many applications. Since kerf loss is minimized, LNC may be desirable for faceting diamond gems or cutting tools. The large, perfectly flat (111) atomic planes are believed to be ideal for stabilizing the spin and electronic properties of sub-surface quantum sensors for nanoscale magnetic resonance imaging [51]. Additionally, the LNC process has potential for reducing or completely eliminating plate wedge, which adversely affects diamond photonic devices [9, 10, 19, 52]. In addition to generating (111)-faced SCD substrates for diamond electronics, photonics, and quantum technologies, LNC will also prove useful for fabricating seed crystals required for improving CVD growth of customized [111]-oriented samples [2, 4, 28, 36, 37, 53].

5. Conclusion

We have demonstrated a new process for fabricating (111)-faced SCD plates by laser-nucleated cleaving. Multiple plates with thicknesses down to 170 μm and face areas up to 3.0 mm \times 0.4 mm are reliably produced from (100) SG crystals with starting dimensions 3.0 mm \times 3.0 mm \times 0.3 mm. The plates exhibit micron-scale atomically-flat terraces, with large areas (up to 1.0 mm \times 0.4 mm) unmarred by laser damage. With the ability to produce large (111) faces out

of commercially available CVD diamond plates comes the opportunity for further exploration of, and access to, SCD as an integral component in high-power electronics, architectures for quantum computing and quantum communication, and ultra-sensitive magnetometers.

Acknowledgements

We thank S. Szewczyk for assistance with X-ray diffraction measurements; B. Peterson and E. Johnston for assistance with micromachining lasers; and A. L. Exharos, T.-Y. Huang, and J. Tabeling for their insightful discussions and comments. This work was supported by an NSF CAREER grant (ECCS-1553511) and the Singh Center for Nanotechnology at the University of Pennsylvania.

References

References

- [1] R. S. Balmer, J. R. Brandon, S. L. Clewes, H. K. Dhillon, J. M. Dodson, I. Friel, P. N. Inglis, T. D. Madgwick, M. L. Markham, T. P. Mollart, N. Perkins, G. A. Scarsbrook, D. J. Twitchen, A. J. Whitehead, J. J. Wilman, S. M. Woollard, Chemical vapour deposition synthetic diamond: materials, technology and applications, *Journal of Physics: Condensed Matter* 21 (36) (2009) 364221. doi:10.1088/0953-8984/21/36/364221.
- [2] J. Gracio, Q. Fan, J. Madaleno, Diamond growth by chemical vapour deposition, *Journal of Physics D: Applied Physics* 43 (37) (2010) 374017. doi:10.1088/0022-3727/43/37/374017.
- [3] The Element Six CVD diamond handbook, https://e6cvd.com/media/wysiwyg/pdf/E6_CVD_Diamond_Handbook_A5_v10X.pdf (December 12, 2017).
- [4] N. Tokuda, Homoepitaxial Diamond Growth by Plasma-Enhanced Chemical Vapor Deposition, Springer International Publishing, 2015, pp. 1–29. doi:10.1007/978-3-319-09834-0_1.
- [5] J. Achard, F. Silva, R. Issaoui, O. Brinza, A. Tallaire, H. Schneider, K. Isoird, H. Ding, S. Koné, M. Pinault, et al., Thick boron doped diamond single crystals for high power electronics, *Diamond and Related Materials* 20 (2) (2011) 145–152. doi:10.1016/j.diamond.2010.11.014.
- [6] T. Makino, K. Yoshino, N. Sakai, K. Uchida, S. Koizumi, H. Kato, D. Takeuchi, M. Ogura, K. Oyama, T. Matsumoto, et al., Enhancement in emission efficiency of diamond deep-ultraviolet light emitting diode, *Appl. Phys. Lett.* 99 (6) (2011) 061110. doi:10.1063/1.3625943.
- [7] A. Balducci, M. Marinelli, E. Milani, M. Morgada, A. Tucciarone, G. Verona-Rinati, M. Angelone, M. Pillon, Extreme ultraviolet single-crystal diamond detectors by chemical vapor deposition, *Applied Physics Letters* 86 (19) (2005) 193509. doi:10.1063/1.1927709.
- [8] R. P. Mildren, J. E. Butler, J. R. Rabeau, CVD-diamond external cavity raman laser at 573 nm, *Opt. Express* 16 (23) (2008) 18950–18955. doi:10.1364/OE.16.018950.
- [9] B. Hausmann, I. Bulu, V. Venkataraman, P. Deotare, M. Lončar, Diamond nonlinear photonics, *Nature Photon.* 8 (5) (2014) 369–374. doi:10.1038/nphoton.2014.72.
- [10] P. Latawiec, V. Venkataraman, M. J. Burek, B. J. Hausmann, I. Bulu, M. Lončar, On-chip diamond raman laser, *Optica* 2 (11) (2015) 924–928. doi:10.1364/OPTICA.2.000924.
- [11] D. M. Toyli, L. C. Bassett, B. B. Buckley, G. Calusine, D. D. Awschalom, Engineering and quantum control of single spins in semiconductors, *MRS Bulletin* 38 (2013) 139–143. doi:10.1557/mrs.2013.21.

- [12] G. Balasubramanian, A. Lazariev, S. R. Arumugam, D.-W. Duan, Nitrogen-vacancy color center in diamond-emerging nanoscale applications in bioimaging and biosensing, *Current opinion in chemical biology* 20 (2014) 69–77. doi:10.1016/j.cbpa.2014.04.014.
- [13] R. J. Narayan, R. D. Boehm, A. V. Sumant, Medical applications of diamond particles & surfaces, *Materials today* 14 (4) (2011) 154–163. doi:10.1016/S1369-7021(11)70087-6.
- [14] L. Rondin, J. Tetienne, T. Hingant, J. Roch, P. Maletinsky, V. Jacques, Magnetometry with nitrogen-vacancy defects in diamond, *Reports on Progress in Physics* 77 (5) (2014) 056503. doi:10.1088/0034-4885/77/5/056503.
- [15] I. Aharonovich, A. D. Greentree, S. Praver, Diamond photonics, *Nature Photonics* 5 (7) (2011) 397–405. doi:10.1038/nphoton.2011.54.
- [16] I. Aharonovich, E. Neu, Diamond nanophotonics, *Advanced Optical Materials* 2 (10) (2014) 911–928. doi:10.1002/adom.201400189.
- [17] T. Schröder, S. L. Mouradian, J. Zheng, M. E. Trusheim, M. Walsh, E. H. Chen, L. Li, I. Bayn, D. Englund, Quantum nanophotonics in diamond [invited], *JOSA B* 33 (4) (2016) B65–B83. doi:10.1364/JOSAB.33.000B65.
- [18] R. R. Grote, L. C. Bassett, Single-mode optical waveguides on native high-refractive-index substrates, *APL Photonics* 1 (7) (2016) 071302. doi:10.1063/1.4955065.
- [19] F. Gao, Z. Huang, B. Feigl, J. Van Erps, H. Thienpont, R. G. Beausoleil, N. Vermeulen, Low-loss millimeter-length waveguides and grating couplers in single-crystal diamond, *J. Light-wave Technol.* 34 (23) (2016) 5576–5582. doi:10.1109/JLT.2016.2622620.
- [20] E. M. Wilks, J. Wilks, The resistance of diamond to abrasion, *Journal of Physics D: Applied Physics* 5 (10) (1972) 1902. doi:10.1088/0022-3727/5/10/323.
- [21] J. Field, The mechanical and strength properties of diamond, *Reports on Progress in Physics* 75 (12) (2012) 126505. doi:10.1088/0034-4885/75/12/126505.
- [22] R. P. Mildren, A. Sabella, O. Kitzler, D. J. Spence, A. M. McKay, Diamond raman laser design and performance, *Optical Engineering of Diamond* (2013) 239–276. doi:10.1002/9783527648603.ch8.
- [23] A. Sabella, J. A. Piper, R. P. Mildren, 1240 nm diamond raman laser operating near the quantum limit, *Opt. Lett.* 35 (23) (2010) 3874–3876. doi:10.1364/OL.35.003874.
- [24] M. Katagiri, J. Isoya, S. Koizumi, H. Kanda, Lightly phosphorus-doped homoepitaxial diamond films grown by chemical vapor deposition, *Appl. Phys. Lett.* 85 (26) (2004) 6365–6367. doi:10.1063/1.1840119.
- [25] H. Kato, S. Yamasaki, H. Okushi, n-type doping of (001)-oriented single-crystalline diamond by phosphorus, *Appl. Phys. Lett.* 86 (22) (2005) 222111. doi:10.1063/1.1944228.
- [26] H. Kato, J. Barjon, N. Habka, T. Matsumoto, D. Takeuchi, H. Okushi, S. Yamasaki, Energy level of compensator states in (001) phosphorus-doped diamond, *Diamond and Related Materials* 20 (7) (2011) 1016–1019. doi:10.1016/j.diamond.2011.05.021.
- [27] H. Kato, M. Ogura, T. Makino, D. Takeuchi, S. Yamasaki, N-type control of single-crystal diamond films by ultra-lightly phosphorus doping, *Applied Physics Letters* 109 (14) (2016) 142102. doi:10.1063/1.4964382.
- [28] A. Tallaire, J. Achard, A. Boussadi, O. Brinza, A. Gicquel, I. Kupriyanov, Y. Palyanov, G. Sakr, J. Barjon, High quality thick CVD diamond films homoepitaxially grown on (111)-oriented substrates, *Diamond and Related Materials* 41 (2014) 34–40. doi:10.1016/j.diamond.2013.11.002.
- [29] D. D. Awschalom, L. C. Bassett, A. S. Dzurak, E. L. Hu, J. R. Petta, Quantum spintronics: engineering and manipulating atom-like spins in semiconductors, *Science* 339 (6124) (2013) 1174–1179. doi:10.1126/science.1231364.
- [30] C. Hepp, T. Müller, V. Waselowski, J. N. Becker, B. Pingault, H. Sternschulte, D. Steinmüller-Nethl, A. Gali, J. R. Maze, M. Atatüre, C. Becher, Electronic structure of the silicon vacancy color center in diamond, *Phys. Rev. Lett.* 112 (2014) 036405. doi:10.1103/PhysRevLett.112.036405.
- [31] M. K. Bhaskar, D. D. Sukachev, A. Sipahigil, R. E. Evans, M. J. Burek, C. T. Nguyen, L. J. Rogers, P. Siyushev, M. H. Metsch, H. Park, F. Jelezko, M. Lončar, M. D. Lukin, Quantum nonlinear optics with a germanium-vacancy color center in a nanoscale diamond waveguide, *Phys. Rev. Lett.* 118 (2017) 223603. doi:10.1103/PhysRevLett.118.223603.
- [32] E. Neu, P. Appel, M. Ganzhorn, J. Miguel-Sánchez, M. Lesik, V. Mille, V. Jacques, A. Tallaire, J. Achard, P. Maletinsky, Photonic nano-structures on (111)-oriented diamond, *Appl. Phys. Lett.* 104 (15) (2014) 153108. doi:10.1063/1.4871580.
- [33] H. Bernien, B. Hensen, W. Pfaff, G. Koolstra, M. S. Blok, L. Robledo, T. H. Taminiau, M. Markham, D. J. Twitchen, L. Childress, R. Hanson, Heralded entanglement between solid-state qubits separated by three metres, *Nature* 497 (7447) (2013) 86–90. doi:10.1038/nature12016.
- [34] L. M. Pham, N. Bar-Gill, D. Le Sage, C. Belthangady, A. Stacey, M. Markham, D. J. Twitchen, M. D. Lukin, R. L. Walsworth, Enhanced metrology using preferential orientation of nitrogen-vacancy centers in diamond, *Phys. Rev. B* 86 (2012) 121202. doi:10.1103/PhysRevB.86.121202.
- [35] H. Ozawa, K. Tahara, H. Ishiwata, M. Hatano, T. Iwasaki, Formation of perfectly aligned nitrogen-vacancy-center ensembles in chemical-vapor-deposition-grown diamond (111), *Appl. Phys. Express* 10 (4) (2017) 045501. doi:10.7567/APEX.10.045501.
- [36] I. Friel, S. Clewes, H. Dhillon, N. Perkins, D. Twitchen, G. Scarsbrook, Control of surface and bulk crystalline quality in single crystal diamond grown by chemical vapour deposition, *Diamond and Related Materials* 18 (58) (2009) 808 – 815, proceedings of Diamond 2008, the 19th European Conference on Diamond, Diamond-Like Materials, Carbon Nanotubes, Nitrides and Silicon Carbide. doi:10.1016/j.diamond.2009.01.013.
- [37] C. Widmann, M. Hetzl, S. Drieschner, C. Nebel, Homoepitaxial growth of high quality (111)-oriented single crystalline diamond, *Diamond and Related Materials* 72 (2017) 41 – 46. doi:10.1016/j.diamond.2016.12.020.
- [38] S. Stoupin, S. Antipov, J. E. Butler, A. V. Kolyadin, A. Kastrusha, Large-surface-area diamond (111) crystal plates for applications in high-heat-load wavefront-preserving X-ray crystal optics, *Journal of Synchrotron Radiation* 23 (5) (2016) 1118–1123. doi:10.1107/S1600577516011796.
- [39] J. R. Hird, Polishing and shaping of monocrystalline diamond (2013) 71–107. doi:10.1002/9783527648603.ch3.
- [40] V. I. Konov, T. V. Kononenko, V. V. Kononenko, *Laser Micro- and Nanoprocessing of Diamond Materials*, Wiley Online Library, 2013, pp. 385–443. doi:10.1002/9783527648603.ch12.
- [41] M. Kumagai, N. Uchiyama, E. Ohmura, R. Sugiyama, K. Atsumi, K. Fukumitsu, Advanced dicing technology for semiconductor waferstealth dicing, *IEEE Transactions on Semiconductor Manufacturing* 20 (3) (2007) 259–265. doi:10.1109/TSM.2007.901849.
- [42] See the supporting information available online.
- [43] Element six, <https://e6cvd.com/us/> (December 12, 2017).
- [44] V. I. Konov, *Laser in micro and nanoprocessing of diamond materials*, *Laser & Photonics Reviews* 6 (6) (2012) 739–766. doi:10.1002/lpor.201100030.
- [45] A. Rabinovitch, V. Frid, D. Bahat, Wallner lines revisited, *J. Appl. Phys.* 99 (2006) 076102. doi:10.1063/1.2181692.
- [46] Applied diamond, inc., <http://usapplieddiamond.com/> (December 12, 2017).
- [47] T. Kononenko, V. Konov, S. Pimenov, N. Rossukany, A. Rukovichnikov, V. Romano, Three-dimensional laser writing in diamond bulk, *Diamond and Related Materials* 20 (2) (2011) 264–268. doi:10.1016/j.diamond.2010.12.013.
- [48] R. H. Telling, C. J. Pickard, M. C. Payne, J. E. Field, Theoretical strength and cleavage of diamond, *Phys. Rev. Lett.* 84 (2000) 5160–5163. doi:10.1103/PhysRevLett.84.5160.
- [49] E. Ohmura, M. Kumagai, M. Nakano, K. Kuno, K. Fukumitsu, H. Morita, Analysis of processing mechanism in stealth dicing of ultra thin silicon wafer, *Journal of Advanced Mechan-*

- ical Design, Systems, and Manufacturing 2 (4) (2008) 540–549. doi:[10.1299/jamdsm.2.540](https://doi.org/10.1299/jamdsm.2.540).
- [50] R. Casquel, M. Holgado, J. García-Ballesteros, K. Zinoviev, C. Fernández-Sánchez, F. Sanza, C. Molpeceres, M. Laguna, A. Llobera, J. Ocaña, et al., Uv laser-induced high resolution cleaving of Si wafers for micro–nano devices and polymeric waveguide characterization, *Applied Surface Science* 257 (12) (2011) 5424–5428. doi:[10.1016/j.apsusc.2010.11.021](https://doi.org/10.1016/j.apsusc.2010.11.021).
 - [51] J.-P. Chou, A. Retzker, A. Gali, Nitrogen-terminated diamond (111) surface for room-temperature quantum sensing and simulation, *Nano Letters* 17 (4) (2017) 2294–2298. doi:[10.1021/acs.nanolett.6b05023](https://doi.org/10.1021/acs.nanolett.6b05023).
 - [52] B. J. Hausmann, I. Bulu, P. Deotare, M. McCutcheon, V. Venkataraman, M. Markham, D. Twitchen, M. Lončar, Integrated high-quality factor optical resonators in diamond, *Nano Lett.* 13 (5) (2013) 1898–1902. doi:[10.1021/nl3037454](https://doi.org/10.1021/nl3037454).
 - [53] K. Ohno, F. J. Heremans, L. C. Bassett, B. A. Myers, D. M. Toyli, A. C. B. Jayich, C. J. Palmstrøm, D. D. Awschalom, Engineering shallow spins in diamond with nitrogen delta-doping, *Appl. Phys. Lett.* 101 (8) (2012) 082413. doi:[10.1063/1.4748280](https://doi.org/10.1063/1.4748280).

Supporting Information for “Fabrication of (111)-Faced Single-Crystal Diamond Plates by Laser Nucleated Cleaving”

Samuel M. Parks^a, Richard R. Grote^a, David A. Hopper^{a,b}, Lee C. Bassett^{a,*}

^aQuantum Engineering Laboratory, Department of Electrical & Systems Engineering,
University of Pennsylvania, Philadelphia, PA 19104, United States

^bDepartment of Physics, University of Pennsylvania, Philadelphia, PA 19104, United States

1. Sample details

Details regarding the single-crystal diamond (SCD) starting plates as provided by the manufacturer [1] are provided in Table S1. The edge and face orientations of both standard grade (SG) and electronics grade (EG) starting plates are depicted in Fig. 1(c,d) of the main text.

	Electronics grade	Standard grade
N content	< 5 ppb	< 1 ppm
B content	< 1 ppb	< 0.05 ppm
Lateral Dims.	2.0 mm × 2.0 mm	3.0 mm × 3.0 mm
Thickness	0.5 mm	0.3 mm
Part no.	145-500-0385	145-500-0253

Table S1: Type IIa CVD-grown SCD starting plate specifications from Element6 [1].

2. Micromachining laser details

Specifications for the laser micromachining tools used for LNC are given in Table S2. The 193 nm excimer laser tool was used to pattern cleave nucleation sites on the bottom surface of double-side polished samples, while the 532 nm Yb-doped fiber laser tool was used for initiating and propagating cleaves. The spot size of the excimer laser is defined by a variable aperture, which is set here to a 10 $\mu\text{m} \times 10 \mu\text{m}$ square mask.

2.1. Finding and setting focus

The focus of the 532 nm laser is found by setting the laser power to 100% with a repute of 150 kHz and attempting to ablate the surface at different stage heights. The results of this calibration can be seen in Fig. S1. The minimum ablated spot diameter gives us an upper bound on the beam waist of 17 μm , however the exact value is difficult to measure due to the nonlinear nature of the ablation process. The laser focus is determined to be the

	Excimer	Yb-doped fiber
Model	IX-255	IX-280-ML
Wavelength	193 nm	532 nm
Max Pulse energy	800 μJ	200 μJ
Max Rep. rate	120 Hz	300 kHz
Pulse Length	10 ns	2 ns
Min Spot diam.	10 μm (apertured)	<17 μm
Max Fluence	25 J/cm ²	90 J/cm ²

Table S2: Specifications for the micromachining lasers used (IPG Photonics).

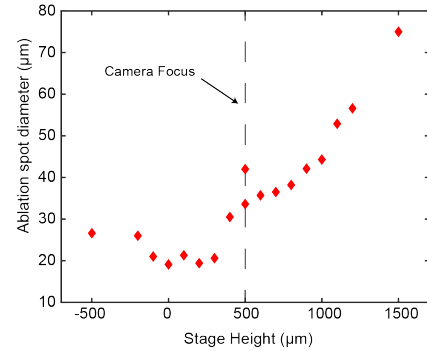


Figure S1: Ablation spot diameter on the top polished diamond surface for varying stage heights. Increasing stage height corresponds to the sample surface being translated towards the laser focusing lens.

stage height producing the minimum ablated region width. In our coordinate system, increasing stage heights imply that the sample is being translated closer to the focusing lens. We found that the inspection camera focus and the laser focus differed by $\approx 500 \mu\text{m}$ and that care had to be taken to position the diamond sample in the proper location such that the top face was below the ablation threshold as is seen in Figure 3 of the main text. This calibration is performed before every cleave process to ensure that the sample is positioned properly.

2.2. Ablation rate

The ablation rate as a function of pulse energy in Fig. 3 of the main text was measured by setting the top dia-

*Corresponding author.

Email address: lbassett@seas.upenn.edu (Lee C. Bassett)

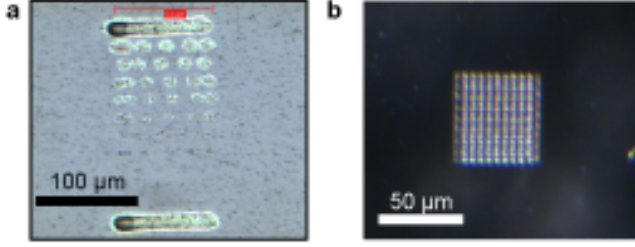


Figure S2: (a) Region used for measuring ablation rate in figure 3 of the main text. (b) Nucleation site fabricated using the UV Excimer laser [Tab. S2].

mond surface at the point of laser focus, fixing the laser rep rate at 150 kHz, and linearly varying the laser pulse energy between 10 μ J and 200 μ J in 10 steps with a variable attenuator to produce the series of ablation sites shown in Fig. S2(a). Five exposures at each pulse energy were performed and averaged to arrive at the measured depth of the resulting ablation site, which were measured by AFM.

2.3. Creating the nucleation site

The textured nucleation site shown in the main text [Fig. 2(a)] is fabricated using an Excimer laser [Tab. S2]. The nucleation site is fabricated on the bottom surface of the SCD plate (see main text for surface name convention). A 50 μ m \times 50 μ m area of ablated diamond [Fig. S2(b)] is created by rastering the 10 μ m \times 10 μ m aperture mask in steps of 5 μ m in two perpendicular directions. The roughened region produced is then suitable for nucleating a cleave.

3. Processing details

3.1. Cleaving Single-Side Polished SG-SCD

The unpolished-surface of single-side polished (SSP) starting plates allowed for the formation (111)-oriented SG-SCD plates without the need for a nucleation site. We found that a scribe line could be cut into the rough back-side using selective ablation that allows for a cleave to propagate the length of the sample unhindered, producing (111) faces unmarred by cleave lines for > 2 mm. This procedure, outlined in Figure S3, requires that the roughened surface be placed on the bottom. A scribe line is then created on the bottom surface, oriented along the desired crystal plane, using the selective ablation procedure with the laser rep rate set at 75 kHz (half the normal operating rep rate of 150 kHz). Following creation of the scribe line, the laser is rastered across 3-5 lines separated by $\approx 212 \mu$ m at 100% power [Fig. S3(a)]. The first raster initiates the cleave, and the subsequent lines propagate the cleave across the entire scribe line to the sample edge.

3.2. Controlling plate thickness

The (111)-faced SCD plate thickness is chosen by considering the distance between the two desired crystal faces,

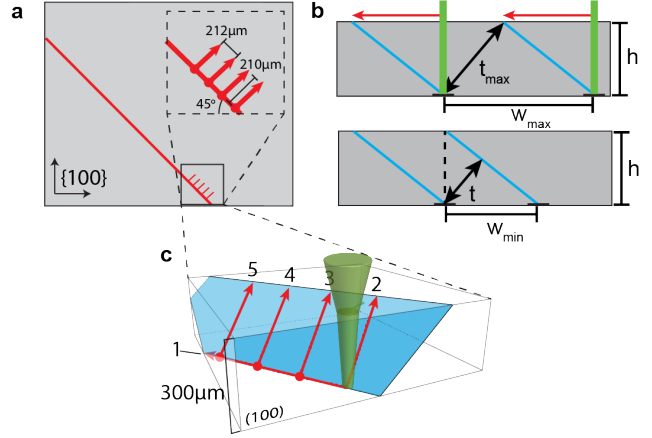


Figure S3: Illustration of the cleaving process (a) Orientation of the scribe line cut with respect to the standard orientation of SG-SCD (b) Side-on profile view of the process for cleaving a {111} plate with parallel faces. w_{\max} denotes the maximum lateral separation between nucleation sites, t_{\max} denotes the maximum plate thickness, w_{\min} denotes the minimum lateral separation between nucleation sites, and t denotes the minimum plate thickness. (c) Expanded image of the set of cleaves required for the scribe-assisted SG-SCD cleaving process.

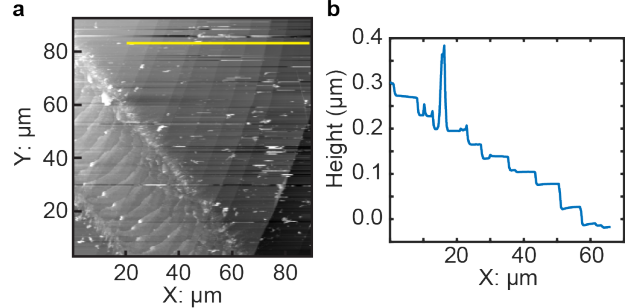


Figure S4: (a) Atomic force micrograph of cleaved (111) face. A portion of the ablated region after a cleave propagation line is seen in the bottom left corner, and a line trace is specified in yellow near the top, seen in (b). (b) Line trace of a cleaved (111) face.

t , and then selecting the appropriate distance between nucleation sites, w , as shown in Fig. S3(b). We generally observe that the laser cannot generate or propagate a cleave when intersecting a previously-created crystal face. Hence the minimum plate thickness we can reliably produce is given by $t_{\min} = h \cos(55^\circ)$, where h is the sample thickness. We occasionally generate thinner samples by accident, and we anticipate that by performing the cleaves on alternating sides of the diamond, thinner plates could be obtained by this method. The maximum thickness that results in two parallel, overlapping (111) faces is also shown in Fig. S3(b).

4. Surface topography analysis

4.1. Power spectral density

Power spectral density (PSD) analysis of the surfaces of LNC fabricated (111) plates is used to characterize the surface roughness at distinct length scales of topographical features relevant for the various uses of LNC SCD (111) plates. The PSD can be integrated in the spatial frequency domain to infer roughness characteristics for a given length scale [2]. Peaks in a given PSD curve correspond to distinct frequencies of roughness, and their heights are related to their contribution to the RMS roughness at that spatial frequency.

We start with the discrete inverse and forward discrete Fourier transforms describing the surface topography, h_x :

$$h_x = \frac{1}{L_x} \sum_q \tilde{h}_q e^{iqx} \quad (1)$$

$$\tilde{h}_q = l_x \sum_x h_x e^{-iqx}, \quad (2)$$

where L_x is the length of the AFM scan in the x-direction, q is the vector of spatial frequencies, and l_x is the pixel size of the AFM scan, $l_x = N_x/L_x$ where N_x is the number of points across a single horizontal line scan. The PSD of the topography above is then defined as

$$C_q^{1D} = L_x^{-1} |\tilde{h}_q|^2 \quad (3)$$

It follows that Eq. 3 is related to the RMS roughness (R_q) by

$$R_q = \sqrt{L_x^{-1} \sum_q C_q^{1D}} \quad (4)$$

To calculate the PSD, for a given AFM scan, we use the fast Fourier transform (FFT) algorithm to calculate the Fourier components h_q and corresponding PSD for each line scan of the image, and then average them together to calculate the PSD for the full image. No image adjustments or corrections have been applied to the AFM data prior to this analysis. Note that, as calculated, the PSD only reflects spatial frequencies in the (horizontal) x -direction of each AFM image, so the specific shape of the curve can depend on the orientation of the image relative to specific sample features. However, the integrated value of the RMS roughness is independent of sample orientation.

4.2. Miscut measurement

We estimate the miscut of LNC-fabricated (111) plates using large-scale AFM scans. Figure S4 is a typical example of a region on cleaved (111) surfaces exhibiting Wallner lines. The miscut angle is calculated by counting the number and height of steps in line scans such as in Fig. S4(b). In those data, a distance of 67 μm was scanned with a total vertical offset of 0.31 μm , corresponding to a miscut angle of $\tan^{-1}(0.31/67) = 0.27^\circ$.

References

- [1] Element six, <https://e6cvd.com/us/> (December 12, 2017).
- [2] T. D. Jacobs, T. Junge, L. Pastewka, Quantitative characterization of surface topography using spectral analysis, *Surface Topography: Metrology and Properties* 5 (1) (2017) 013001.